Controllable assembly of single/double-thin-shell g-C3N4 vesicles via a shape-selective solid-state templating method for efficient photocatalysis

Lei Luo[1, 2], Keyan Li[1], Anfeng Zhang[1], Hainan Shi[1], Junwang Tang[2, 3], Chunshan Song[1, 4]*, Xinwen Guo[1]*

[1] State Key Laboratory of Fine Chemicals, PSU-DUT Joint Center for Energy Research, School of Chemical Engineering, Dalian University of Technology, Dalian 116024, P. R. China.

[2] Key Lab of Synthetic and Natural Functional Molecule Chemistry of Ministry of Education, and the Energy and Catalysis Hub, College of Chemistry and Materials Science, Northwest University, Xi'an 710069, P. R. China

[3] Department of Chemical Engineering, University College London, Torrington Place, London WC1E 7JE, UK.

[4] EMS Energy Institute, PSU-DUT Joint Center for Energy Research and Department of Energy & Mineral Engineering, Pennsylvania State University, University Park, Pennsylvania 16802, United States.

Table of Contents

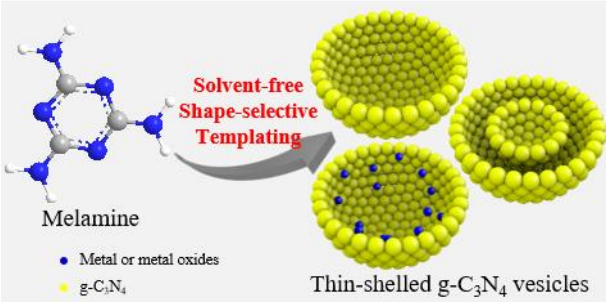

A solvent-free shape-selective templating method has been developed to fabricate the single/double thin-shelled and functional g-C_3N_4 vesicles.

Abstract

Capable of enhanced photoabsorption and redox sites separation, thin-shelled hollow photocatalysts can better match the transport distance of photogenerated carriers but still suffer from preparation difficulty because of the ease of structural collapse. Here, a solvent-free shape-selective templating method has been developed to fabricate the single/double-thin-shelled g-C_3N_4 vesicles. During the solid-solid preparation process, the shape-selectivity of MCM-41 sieves plays a crucial role in the free diffusion and concentration enrichment of melamine precursor, while inhibiting its polymerization inside the channels. The opened-up available outer surface determines the morphology of the vesicles. Uniform shell thickness from 17.5 to 42.1 nm can be precisely controlled. The kinetic constant of double-shelled g-C_3N_4 reaches 0.078 min^{-1}, almost 16 folds of the bulk one during RhB degradation under visible light irradiation. Suppressed charge recombination and enhanced photoabsorption contribute to the improved photocatalytic performance. This newly developed method also shows universality for encapsulation of the secondary component including noble metal and metal oxides in g-C_3N_4.

Keywords

g-C_3N_4, vesicles, solvent-free, photocatalysis

Introduction

Considerable metal and metal-free photocatalysts have been devoted for efficient solar energy utilization, which is an attractive and sustainable solution to relieve the energy consumption and environmental issues[1-4]. Recently, graphitic carbon nitride (g-C_3N_4) has emerged as a metal-free visible-light responsive photocatalyst capable of water splitting[1, 5-9], CO_2 photoreduction[10-12],

nitrogen fixation and pollutant decontamination[13, 14]. Thermal polymerization of various nitrogen-rich precursors[13-23] can fabricate g-C_3N_4 on a large scale, however, still encountered the limited S_{BET} (< 10 m^2/g) and high charge recombination rate. Nanostructural design and electronic structural modification are efficient means to improve photocatalytic performance. The former can not only provide more active sites, but also promote mass transfer and shorten transport length of the photogenerated carriers. The latter can enhance the photoabsorption as well as the charge separation. Hollow structural nanoparticle, taking the advantage of the shell selectivity, pH tolerate capacity and inner actives stability, is a promising structure with versatile applications[24-26]. In the case of photocatalysis, hollow structure prevails because of the shortened charge carrier lengths and light trapping effects inside the cavity[15, 27-30], in addition to a porous structure facilitating the mass transport and high surface area that provides more accessible active sites[31-33]. The thinner the wall is, the easier it is for the charge carriers to transport to the outer surface for efficient utilization.

Hard-templating method is a widely used and efficient route for preparing hollow structures. Hollow g-C_3N_4 with tunable wall thickness was firstly prepared with the core/shell silica templates[27]. Subsequently, multi-shelled g-C_3N_4 hollow structure was prepared through exactly the same method except for the multi-shelled silica templates[15]. As the traditional hard-templating method relies on the reverse porous replication, the precursors should have low melting point or high solubility to facilitate the precursor pre-casting into the channels. The most used precursor for morphological control is cyanamide, which is efficient but expensive and virulent. Furthermore, the pre-casting process results in the complex operation which is time-consumption and energy-wasting. More importantly, the preparation of ultra-thin-walled structure is still difficult through the traditional hard-templating method because of the easy

collapse of the structure. Therefore, the development of facile, economic and reliable method for thin-walled photocatalysts preparation is highly desirable.

The encapsulated structure can not only improve the stability of the inner layer via the chemical tolerance of the exterior[24], but also realize the cascade reaction in organic synthesis[34]. In the case of photocatalysis, precise regulation of the component distribution is of great significance in dividing the redox sites[35-37] and promoting charge carrier separation. The secondary components are usually metals, nonmetals and semiconductors. Modifying g-C_3N_4 with noble metal nanoparticles including platinum, gold and silver can efficiently enhance the photocatalysis through the surface plasmon resonance (SPR) effect. The resonance structure could not only induce the formation of the intensive electromagnetic to promote the charge separation, but also trap the resonant photons efficiently for higher photoabsorption. In addition, the noble metal nanoparticles could also act as the electron sinks, which trap the free electrons and thereafter promote the charge separation.

In this work, a modified solvent-free templating method based on the shape selectivity of the MCM-41 sieves, using melamine as the available precursor, was developed to fabricate the thin-walled g-C_3N_4 vesicles. The proper pore size of MCM-41 allows melamine molecules selectively deposited and polymerized on the opened-up surface but not in the relatively narrow channels. On the premise of retaining the pore structure, single- and double-walled g-C_3N_4 vesicles were successfully prepared by adjusting the number of the opened-up surface. Through this method, the universal encapsulation of metal and metal oxides in vesicle structure is realized simultaneously. The photocatalytic activity of the as-prepared g-C_3N_4 were evaluated by the degradation of RhB and water splitting under visible light irradiation and exhibited an enhanced photocatalysis.

Results and discussion

The solvent-free shape-selective templating strategy was developed to fabricate the thin-shelled g-C_3N_4 vesicles based on a solid-solid polymerization process and the shape selectivity of MCM-41 sieves. Spherical MCM-41[38] with a 2.0 nm pore size distribution (Figure S1) and single opened-up surface were used as the sacrificial templates. Cheap and readily available melamine was used as the precursors.

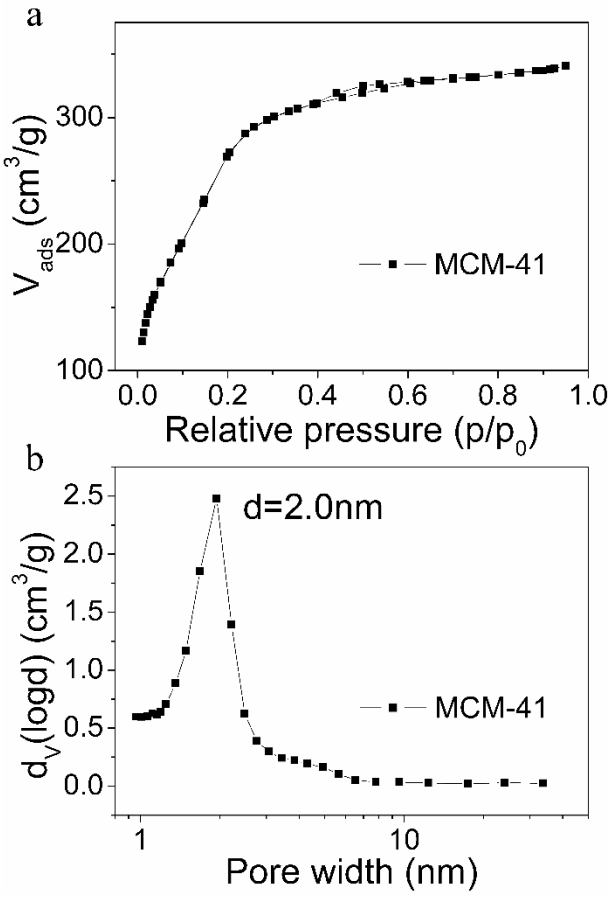

Figure S1. (a) N_2 physical adsorption-desorption isotherms at 77 K and (b) the pore size distribution of MCM-41 calculated by BJH method.

The synthetic process was illustrated in Figure 1a. Through directly calcining the manual grinding mixtures of melamine and MCM-41, followed by thermal polymerization and desilication, single-shelled g-C_3N_4 was prepared and coded as SSCN. Different from the traditional templating method, the thermal sublimation and migration properties of melamine are fully utilized to avoid

the pre-casting process. The solid-solid operation can simplify the operation process while realizing the morphological control. Figure S2 shows the identical MCM-41@g-C_3N_4 nanoparticle at different electron beam radiation time. With the prolongation of irradiation time, the internal structure gradually shrinks, and the voids appear in the particle and gradually increase to 74 nm. The yolk-shell structure not only evidences the initial g-C_3N_4@MCM-41 composite with a core-shell structure but also proves the excellent structural stability of g-C_3N_4. The morphology of SSCN were shown in Figure S2b-c. It can be seen that sample SSCN has a uniform vesicular structure with the wall thickness at ca. 30.0±4.5 nm. The uniform morphology indicates that the formation of bulk morphology by self-template polymerization of melamine is significantly inhibited. Before polymerizing into g-C_3N_4, melamine should undergo a migration to the pore channel or the outer surface, which is a necessary process to realize morphology control without the pre-casting operation. Furthermore, no obvious impurity particles were observed in the cavity, indicating that the polymerization of melamine in the MCM-41 channels was significantly inhibited, otherwise the sample would appear as a porous three-dimensional spherical structure. It is obvious that the spherical MCM-41 plays three roles in the formation of the single-shelled g-C_3N_4: (a) the silica avoids the self-templating polymerization of melamine to bulk morphology, (b) the external surface templates the formation of shell structure, (c) the channel of spherical MCM-41 avoids the polymerization to form the conventional ordered mesoporous materials. As the spherical MCM-41 has a hydroxyl rich surface, the hydrogen bond interaction between the hydroxyl and the amino group of melamine plays a role in enriching the melamine molecules on the surface, enhancing the polymerization and avoiding the self-template to bulk g-C_3N_4. The surface of the spherical MCM-41 can be divided into two parts, including the channel surface and the external surface. As shown in Figure S2, the calculated dynamics diameter of melamine molecular is 0.66 nm, which is

slightly smaller than the pore size distribution of the spherical MCM-41. This indicates the vaporized melamine can freely migrate through the channel of the spherical MCM-41. However, the relatively narrow channel may only accommodate a few molecules, which may form the chain polymer, and hard to form the planar-stacking structure of g-C_3N_4. Moreover, it is quite difficult for the polymerization of such ultralow concentration of melamine in the channels. As a consequence, the polymerization of melamine was restricted within the confined channel surface, in contrast to the external surface of MCM-41 lack of pore restrictions. The key of this strategy lies in the relatively appropriate size of the template channel, the precursor and the product, which is well known as the shape selectivity that widely applied in the shape selective catalysis of zeolite[39]. These phenomena indicate that the polymerization of melamine selectively occurs on the opened-up outer surface of MCM-41.

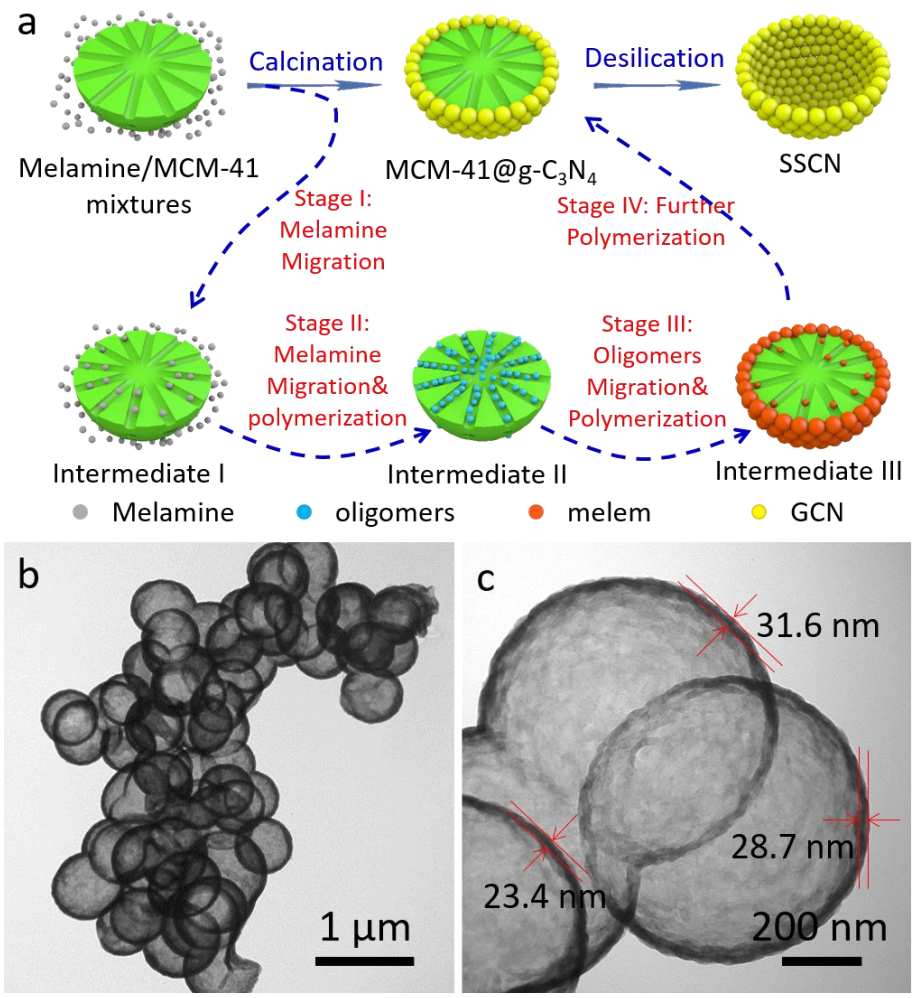

Figure 1. (a) Schematic illustration of the shape-selective templating method for SSCN preparation. (b, c) TEM images of the SSCN.

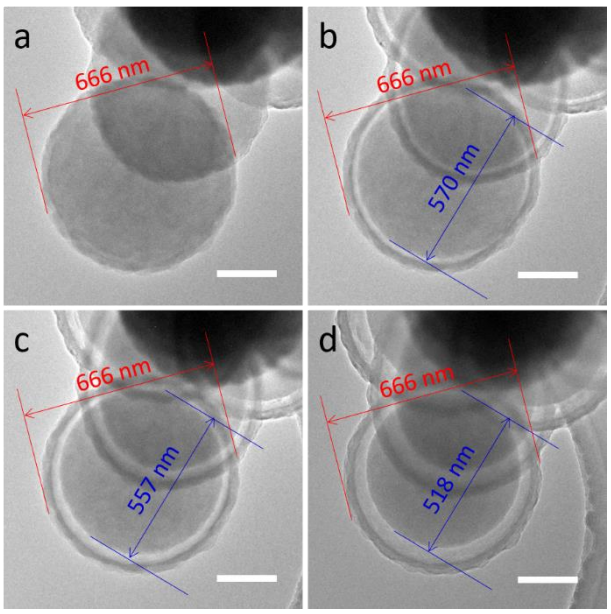

Figure S2. The TEM images of the identical MCM-41@g-C_3N_4 nanoparticle at different electron

beam radiation time. The radiation time is gradually extended from a to d. The scale bar is 200 nm.

Other precursors including dicyanamide and urea were also attempted by this solvent-free method to study the universality, however, it did not exhibit the shape selectivity. A much higher degree of polymerization for the precursor itself is also important which leads to a higher yield of g-C_3N_4. For the dicyanamide and urea precursors with lower degree of polymerization, though the precursors deposit on the surface of the templates, the small molecules would be more active and spread more easily which are unfavorable for the further transition on the surface. Moreover, those precursors generally involves decomposition and repolymerization producing melamine as the intermediate.

The structure and the phase of the as-prepared g-C_3N_4 were identified with X-ray diffraction (XRD) patterns and shown in Figure S3. Bulk g-C_3N_4 (BCN) for comparison was prepared under the identical condition without any templates. For the bulk g-C_3N_4, the typical diffraction peaks at about 27.50^o and 13.04^o are corresponding with the inter-layer structural stacking (200) and the in-planar repeated tri-s-triazine units (100). As a contrast, the single-shelled g-C_3N_4 exhibit a much weakened (200) diffraction peak, which indicates the decreased stacking layers and corresponds with the morphological evolution from bulk to the thin shells. Meanwhile, SSCN also exhibits an absence of the (100) diffraction peak, attributing to the minor fragmental g-C_3N_4 composition which greatly increases the structural chaos of the shells as evidenced by the SEM images.

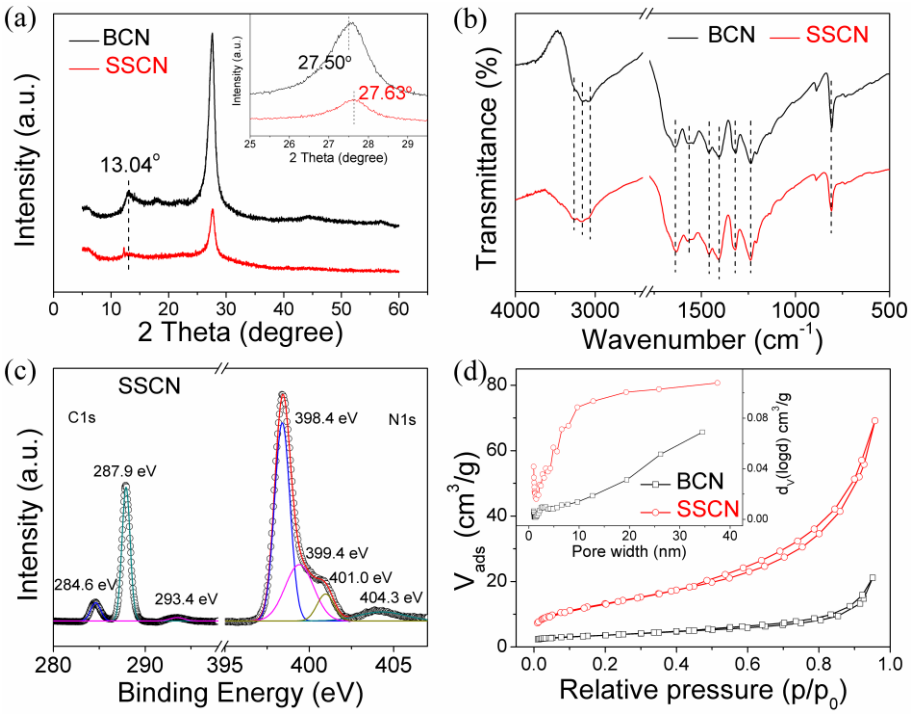

Figure S3. Structure and phase identification of BCN and SSCN. (a) XRD patterns, (b) FT-IR spectra, (c) C1s and N1s high resolution XPS spectra, (d) N_2 physical adsorption-desorption isotherms at 77K and the pore size distribution calculated by BJH method (shown inset).

Fourier transform-infrared (FT-IR) spectra are shown in Figure S3b and prove the typical structure of g-C_3N_4. Series of strong bands at 1200-1600 cm^{-1} and a sharp band at 810 cm^{-1} were attributed to the stretching vibration and breathing mode of the heptazine heterocycle ring (C_6N_7) units of g-C_3N_4. The broad bands at 3000-3600 cm^{-1} are assigned to the N-H and O-H bands, indicating the existence of the uncondensed amino groups and the absorbed water molecular on the surface of the as-prepared g-C_3N_4. Elemental analysis indicates all the three samples composed of carbon and nitride with a C/N molar ratio at ca. 0.67, lower than the ideal g-C_3N_4 composition (C/N=0.75) because of the terminal uncondensed amino groups. X-ray photoelectric spectra (XPS) were conducted to further reveal the chemical composition (Figure S3c). Only three elements (C, N, O) were detected according to the survey XPS spectra. The O1s peak may be attributed to the

surface absorbed oxygen species[40], as confirmed by the FT-IR spectra. The two samples exhibit C1s and N1s signals with a surface C/N ratio at 0.76 and 0.81, close to the ideal g-C_3N_4 composition. Furthermore, the absence of Si signal indicates that the silica templates were totally eliminated with the NH_4HF_2 solution. The high resolution XPS spectra were conducted to further investigate the chemical state of carbon and nitride elements. In the case of the C1s spectra, two distinguished peaks were presented. The smaller peak at 284.6 eV is attributed to the sp^2 C-C bonds and usually used to normalize the XPS spectra. The other prominent peak at 287.9 eV is attributed to the N-C=N bonds in the heptazine heterocycle ring (C_6N_7) units. It is obvious that the latter carbon species is considered as the main carbon species in the g-C_3N_4. The N1s spectra were deconvoluted into four individual peaks at 398.4, 399.3, 401.0 and 404.0 eV, which are assigned to the C-N=C in the triazine ring, the tertiary nitrogen (N-$(C)_3$), the terminal amino groups (-NH_2) and π-excitations, respectively. The above results confirmed the essentially unchanged elemental state and content of g-C_3N_4 under different synthetic conditions.

Nitrogen physical sorption at 77K were conducted to further characterize the textural properties of the as-prepared morphological g-C_3N_4 and shown in Figure S3d and Table S1. As shown in Figure S3d, BCN exhibits type II adsorption isotherm, with a low surface area at 12.8 m^2/g, which is corresponding with the literature[41, 42]. As a comparison, the single-shelled g-C_3N_4 presents an improved surface area of 48.0 m^2/g, as shown in Table S1. Meanwhile, the H3 hysteresis loop indicates that SSCN was composed of fragmental g-C_3N_4 nanosheets, but not a complete ink-bottle structure. Notably, the reason why the hollow structure evidenced by the SEM and TEM did not be reflected in the nitrogen physical sorption is attributed to the large pore size distribution (> 4 nm) of the shells, which results in the unclosed system of the as-prepared hollow structure.

Table S1. Textual properties and elemental composition of samples BCN, SSCN and DSCN.

Sample	C/N[a]	Surface C/N[b]	S_{BET}[c] (m^2/g)	V_{pore}[d] (cm^3/g)
BCN	0.67	0.76	12.8	0.03
SSCN	0.68	0.81	48.0	0.12
DSCN	0.66	0.81	42.4	0.09

a) Elemental analysis, b) XPS spectra, c) BET methods, d) p/p_0=0.95.

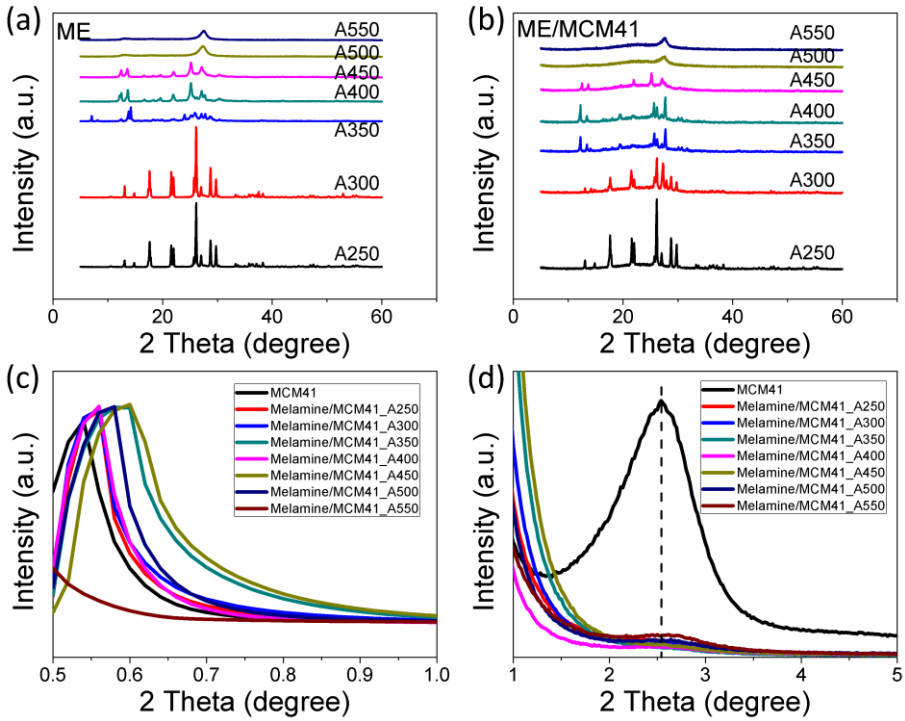

Figure S4. XRD patterns of g-C_3N_4/MCM-41 composites prepared under different temperatures.

To figure out the thermal migration behavior of melamine during the solid phase synthesis, the products calcined with MCM-41 and without MCM-41 at different temperatures were compared. Figure S4 shows the wide-angle and small-angle XRD patterns of the products calcined at different temperatures, with the phase of the products shown in Table S2. As can be seen, with the increase of calcination temperature, melamine gradually polymerized into g-C_3N_4. When the temperature is

lower than 300 ºC, melamine is stable and not polymerized. With the temperature rising to 350 ºC, melamine polymerizes into the oligomers. As the temperature continues to rise to 400-500 ºC, the oligomers further polymerize and form melem. When the temperature is above 500 ºC, melem is further polymerized to form g-C_3N_4 (melon). As a contrast, the products shows a certain difference in the absence of MCM-41. Although melamine would not polymerize before 300 ºC, when the temperature is higher than 350 ºC, it will form melem directly without experiencing the formation of the oligomers,. This phenomenon suggests that MCM-41 can promote the polymerization of melamine. The promoting effect on melamine polymerization may be attributed to the enrichment of melamine caused by capillary condensation of MCM-41 pore system. On the other hand, the change of diffraction peak position of small-angle XRD can reflect whether polymer species migrate into the channel or not. As can be seen from Figure S4c, with the increase of polymerization temperature, the small angle diffraction peak increases first and then decreases, and reaches the maximum at 450 ºC. According to the Bragg's Law ($2d\sin\theta = n\lambda$), the high angle shift of diffraction peak indicates that the pore channel becomes narrower, corresponding to the species migrating into the channel. Correspondingly, when the angle of diffraction peak is decreased, the channel becomes wider and species migrate out of the channel. Combined with wide-angle XRD analysis, the migration of carbon and nitrogen species in the polymerization process is illustrated in Figure S5. The contact between melamine and MCM-41 is weak in the mixtures obtained by manual grinding. With the increase of calcination temperature of the mixtures but lower than 350 ºC, melamine migrates partially into the pore channel of MCM-41. When the temperature was 350-450 ºC, melamine further migrated into the channel and polymerized. At 450 ºC, the channel of MCM-41 are maximally filled with carbon and nitrogen species. Further rising the temperature, carbon and nitrogen species migrate out of the channel and deposit on the opened-up surface. The

driving force of this migration to the outer surface may be attributed to the narrow pores that limit the occurrence of further polymerization inside the channel.

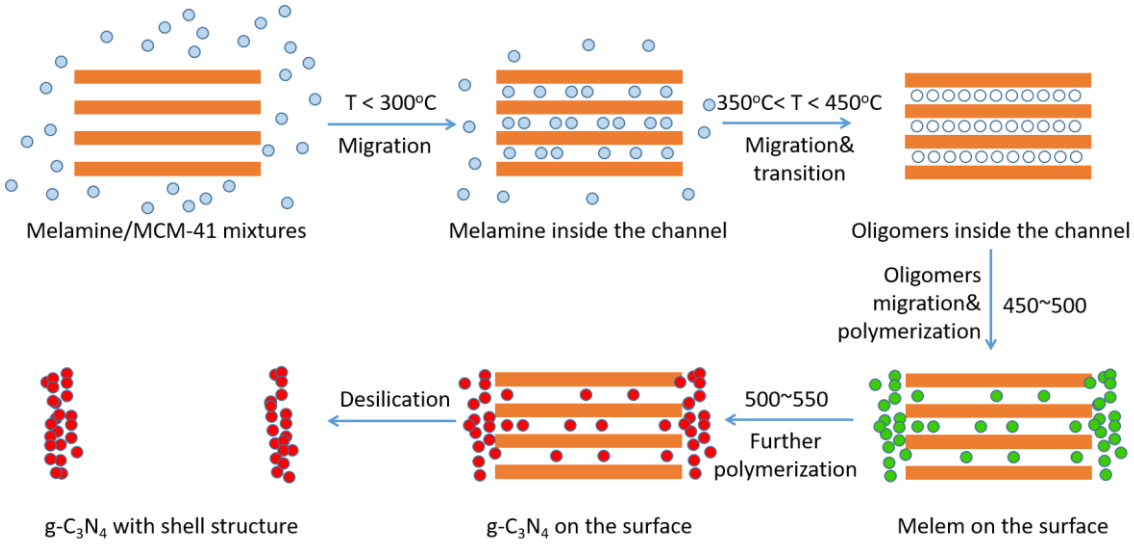

Figure S5. The schematic illustration of the migration and polymerization of the carbon and nitrogen species in the presence of MCM-41.

Table S2. The phase of the products obtained from melamine polymerization with MCM-41 or without MCM-41 at different temperatures.

Temperature (°C)	Phase[a]	
	Without MCM-41	With MCM-41
200	melamine	melamine
250	melamine	melamine
300	melamine	melamine
350	Phase I[b] and II[c]	melem
400	melem	melem

450	melem	melem
500	g-C_3N_4	g-C_3N_4
550	g-C_3N_4	g-C_3N_4

[a] Analysed with XRD, [b] phase I: lower temperature oligomers, [c] phase II: higher temperature oligomers[18].

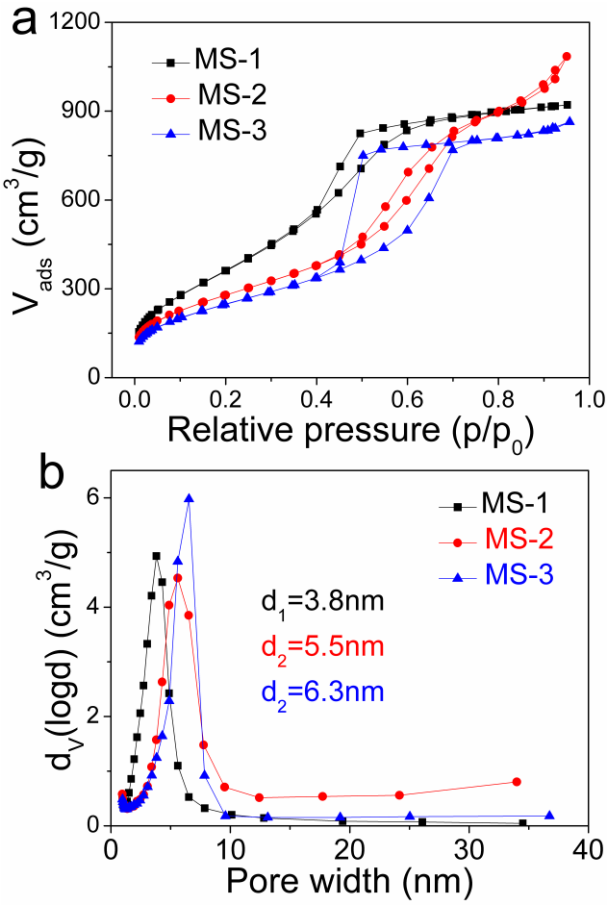

Figure S6. (a, c) Nitrogen physical adsorption-desorption isotherms and (b, d) the pore size distribution of the core/shell silica and series of MS-x silica. The pore size distribution is calculated by the BJH method.

To further identify the role of the appropriate pore size, MCM-41 with larger and tunable channel were used as the templates (coded as MS-x). Figure S6 shows the nitrogen physical sorption isotherms and the pore size distribution of the templates, with the textural properties shown in Table

S3. As can be seen, samples MS-x have tunable pore size distribution, ranging from 3.8 to 6.3 nm, which is much larger than the previous spherical MCM-41. When templating by these larger porous MCM-41, the as-prepared g-C_3N_4 still remains a certain morphology but not bulk (shown in Figure S7), demonstrating that melamine still migrates into the channel of the templates before polymerization. Nevertheless, the larger channel leads to the formation of three-dimensional mesoporous structure, rather than hollow structure, which is mainly because of the disappearance of shape selectivity. In the case of the dense silica with similar particle size, the appearance of bulk morphology (shown in Figure S8) indicates that g-C_3N_4 did not polymerize around the template, which evidenced that the channel of MCM-41 could enrich the precursor to some extent.

Table S3. Textural properties of the core/shell silica and series of MS-x silica.

Sample	S_{BET} (m^2/g)	V_{pore} (cm^3/g)	Pore size (nm)
Core/shell silica	443.2	0.33	2.9
MS-1	1397.5	1.43	3.8
MS-2	1032.3	1.68	5.5
MS-3	923.0	1.34	6.3

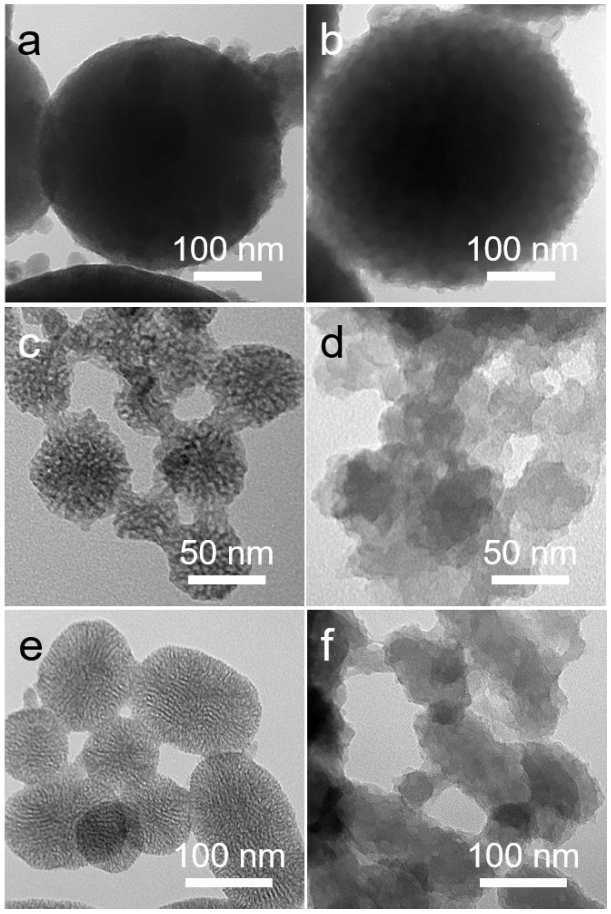

Figure S7. TEM images of (a, c, e) MS-1, MS-2 and MS-3, and (b, d, f) the as-templated g-C_3N_4.

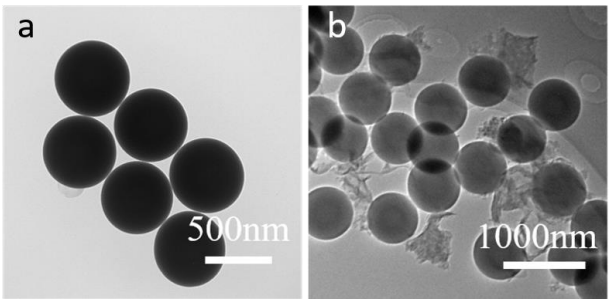

Figure S8. TEM images of (a) dense silica nanoparticles, (b) the products obtained from calcination of the mixtures of dense silica and melamine.

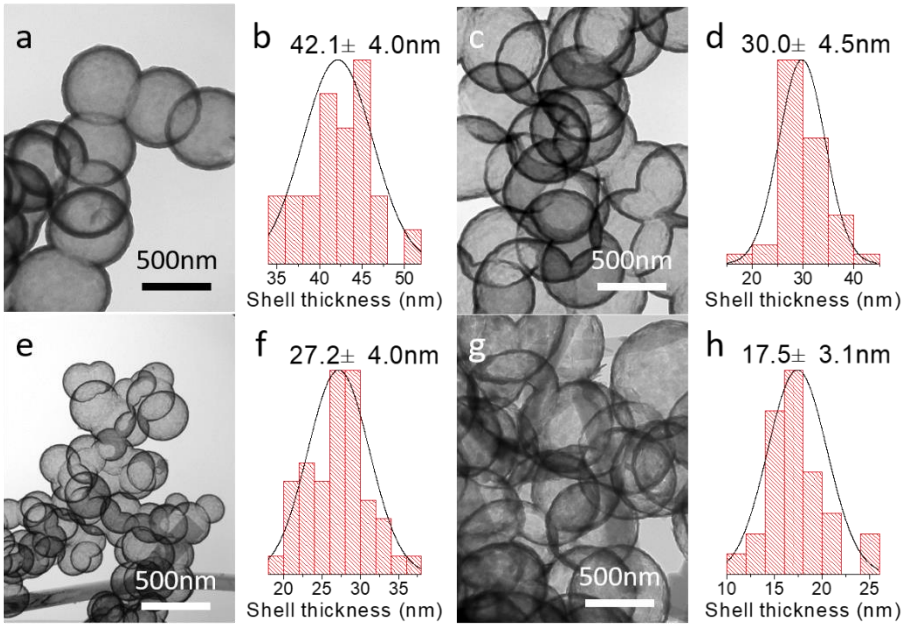

Figure S9. Single-shelled g-C_3N_4 vesicles prepared with different mass ratio of melamine/MCM-41. The ratio is (a) 0.1, (d) 0.3, (e) 0.5, (g) 0.8.

Hollow structure enables the separation of redox active sites on the internal and exterior surfaces, thereafter facilitating the charge separation[35]. The wall thickness of the hollow structure is the shortest distance of photogenerated carrier transport. Therefore, reducing the wall thickness of the hollow structure is beneficial to the migration of photogenerated carriers to the surface. Figure S9 shows the TEM images of g-C_3N_4 vesicles with different wall thickness. By tuning the mass ratio of melamine to MCM-41 between 0.1 and 0.8, the thickness of vesicle structure can be continuously regulated from 42.1 to 17.5 nm. At the same time, because of the unique selective deposition process, the primary nanoparticles composed of the shell are in closer contact with each other, which endows the good structural stability even if its thickness is very thin.

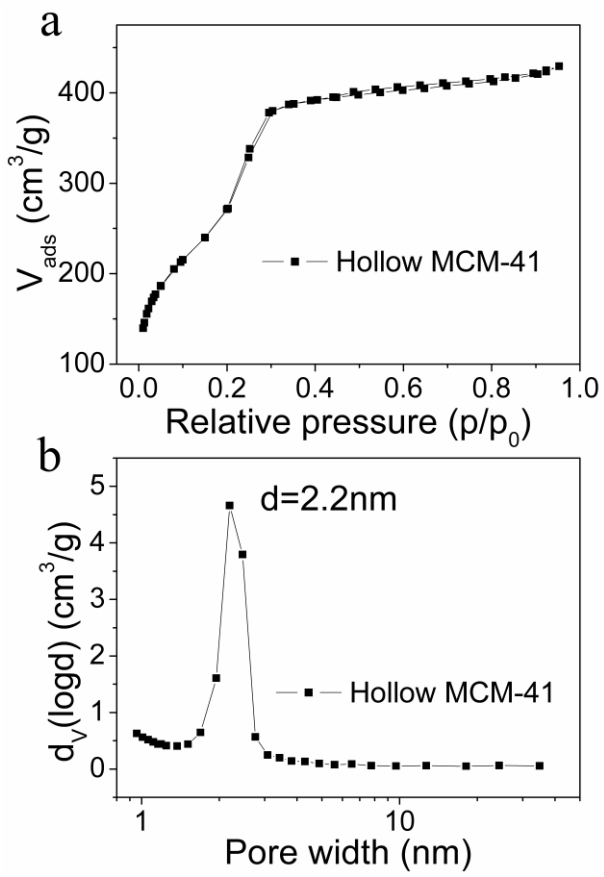

Figure S10. (a) N_2 physical adsorption-desorption isotherms at 77 K and (b) the pore size distribution of hollow MCM-41 calculated by BJH method.

The proper pore size of MCM-41 allows melamine precursor selectively deposited and polymerized on the opened-up surface, therefore, the number of the opened-up surface consequently determines the number of the layers. As reported in the literature, hollow structural photocatalysts exhibit enhanced photoabsorption because of the multi-reflection effect inside the cavity. Multi-walled structure can further enhance the photoabsorption[15, 43]. For constructing the multi-walled structural g-C_3N_4, increase the number of the opened-up surface of MCM-41 maybe sufficient. For instance, the preparation of double-walled structure requires the hollow template with two opened-up surfaces for selective deposition. As a contrast, the same double-walled structure through the conventional method requires the utilization of a three-layer structure template

with two voids for nano-casting. However, the preparation of those three-layer structure templates is difficult. The hollow MCM-41 with a pore size distribution at 2.2 nm(Figure S10) could be facilely prepared by the surface-protected etching method[38], which still remains the shape selectivity for melamine, and the double-shelled g-C_3N_4 (DSCN) vesicles could be prepared using it as the template.

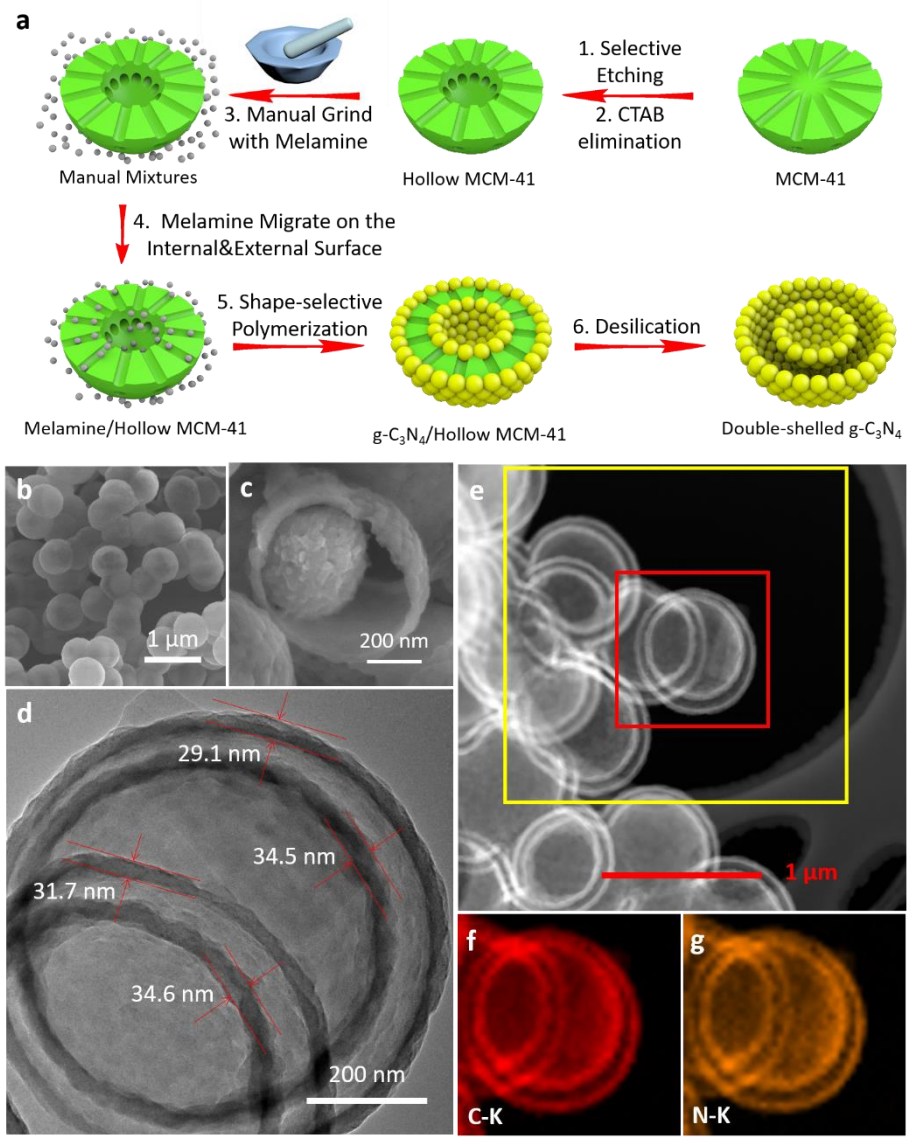

Figure 2. (a) Schematic illustration of the preparation, (b, c) SEM, (d) TEM and (e-g) TEM-mapping images of DSCN.

Figure 2a shows the schematic illustration of the preparation of DSCN vesicles. Through one-step hydrothermal treatment of the previously used MCM-41, hollow MCM-41 was obtained. Manually grinding melamine and hollow MCM-41, followed by calcination and desilication, DSCN was prepared. Figure 2b-c show the SEM images of DSCN. DSCN exhibits a uniform spherical structure without bulk morphology, which confirms that the solvent-free templating strategy can efficiently realize morphology control. The TEM images of the broken DSCN in Figure 2c clearly exhibits the double-walled structure, which composed of primary fragmental nanoparticles. TEM image in Figure 2d further confirms the double-walled vesicle structure, with the interior and exterior wall thickness at ca. 30 nm. Figure 2e-g present the TEM-mapping images of DSCN. It clearly shows the uniform elemental distribution of carbon and nitride, corresponding with the heptazine heterocycle ring (C_6N_7) units of g-C_3N_4.

The photocatalytic properties of the as-prepared g-C_3N_4 were evaluated through the degradation of RhB and H_2 production under visible-light irradiation ($\lambda > 420$ nm). Before turning on the visible light irradiation, the suspension of the photocatalysts and the RhB solution was stirred in dark for 30 min to reach the adsorption-desorption equilibrium. As shown in Figure 3a, all the three evaluation processes reach the adsorption-desorption equilibrium within 30 min and exhibit photocatalytic activity after visible-light irradiation. In the presence of the bulk g-C_3N_4, about 40% of the initial RhB was degraded within 120 min, corresponding with a low first-order kinetic constant at 0.005 min^{-1}. Compared with BCN, SSCN present a photoactivity enhancement and can totally degrade the initial RhB within the same reaction time. The enhanced photoactivity is attributed not only to the enlarged surface area, but also to the suppressed charge recombination efficiency and the enhanced photoabsorption derived from the multiple reflection effect inside the shell. The suppressed charge recombination efficiency originated from the shortened charge carrier

migration length or thinner shell, which makes the photogenerated charge carrier more likely to transfer to the surface and be captured by the RhB substrates.

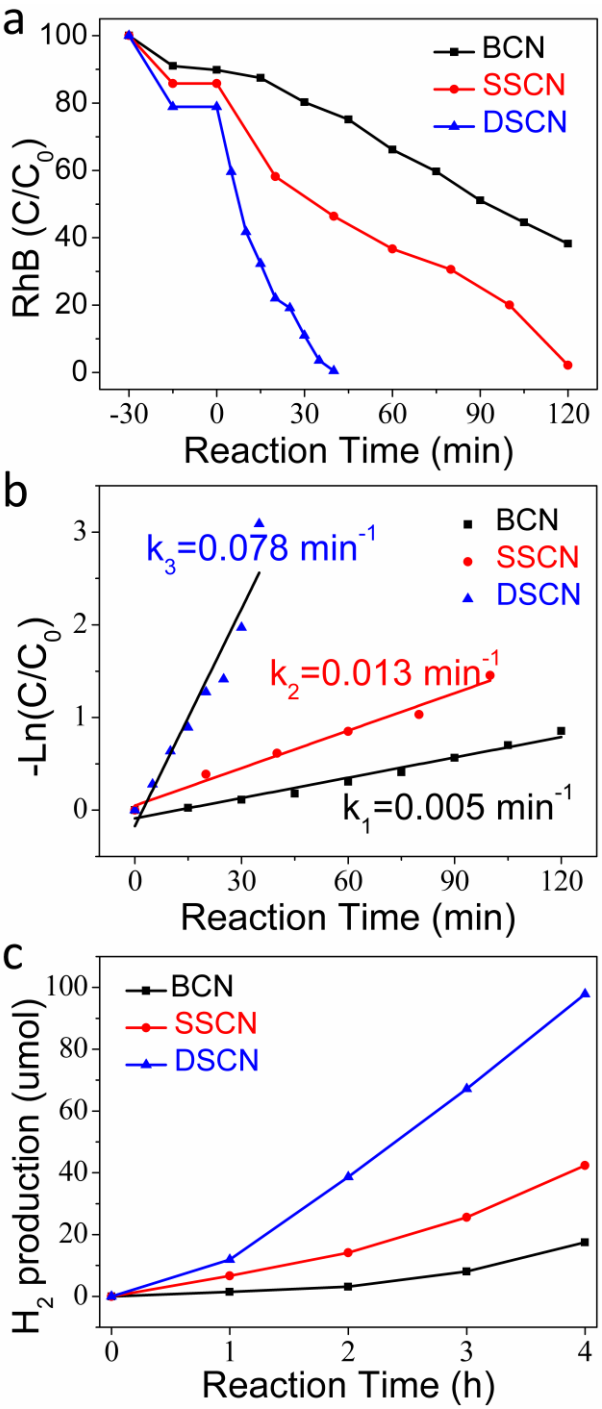

Figure 3. (a) Photocatalytic degradation of RhB, (b) the first-order kinetic constant under visible light irradiation (λ > 420 nm) as a function of the reaction time. Reaction condition: 50 mg photocatalysts, 50 mL RhB solution (50 mg/L). (c) photocatalytic H_2 production of BCN, SSCN

and DSCN under visible light irradiation ($\lambda > 420$ nm).

Further increasing the number of the shell, DSCN presents a superior photoactivity improvement and can totally degrade the initial RhB within 40 min. Compared with the bulk g-C_3N_4 and the single-shell g-C_3N_4, the first-ordered kinetic constant improved almost 15.6 folds. As the surface area of SSCN and DSCN is similar with each other, the further improved photoactivity for DSCN predominantly attributed to the light trapping effect inside the multiple shells. Notably, as the pore size distribution of the shell is larger than the RhB molecular, the surface including the internal shell is always accessible and can be fully utilized for photocatalytic reaction.

Photocatalytic H_2 production was carried under 4 h continuous visible-light irradiation and shown in Figure 3c. With the duration of visible-light irradiation, the amount of the produced H_2 continuously increases, indicating the visible-light photocatalytic activity. Compared with BCN, SSCN and DSCN exhibit a much higher H_2 evolution rate, consistent with that of RhB degradation reaction.

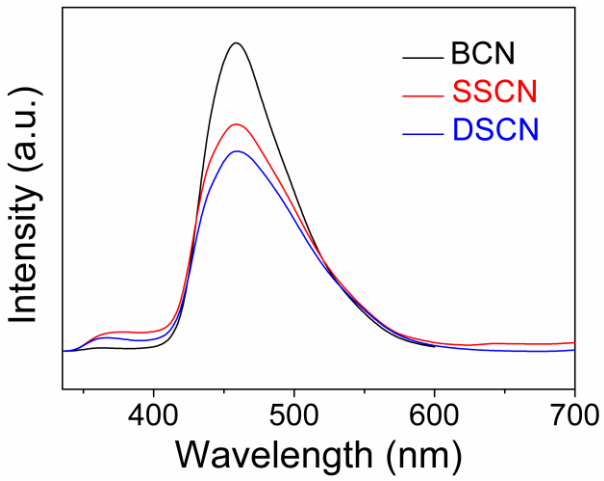

Figure S11. Steady-state photofluorescence spectra of BCN, SSCN and DSCN.

The steady-state photofluorescence (PL) spectra were performed to characterize the photogenerated charge carrier recombination efficiency. As shown in Figure 4d, compared with the

bulk g-C_3N_4, the morphological g-C_3N_4 performed a consecutively weakened PL intensity from SSCN to DSCN. The most weakened PL intensity for DSCN indicates the lowest charge recombination efficiency, which is favorable to the photocatalysis.

Besides morphology control, the novel solvent-free templating strategy can also realize the encapsulation of the secondary component for nano-composite construction. The composite structure of MCM-41 and g-C_3N_4 is a core-shell structure and the channel of MCM-41 is not occupied in the composite structure. Therefore, if a certain amount of the secondary component is placed in the channels of MCM-41 in advance (as shown in Figure S12), the functionalized vesicles will be prepared.

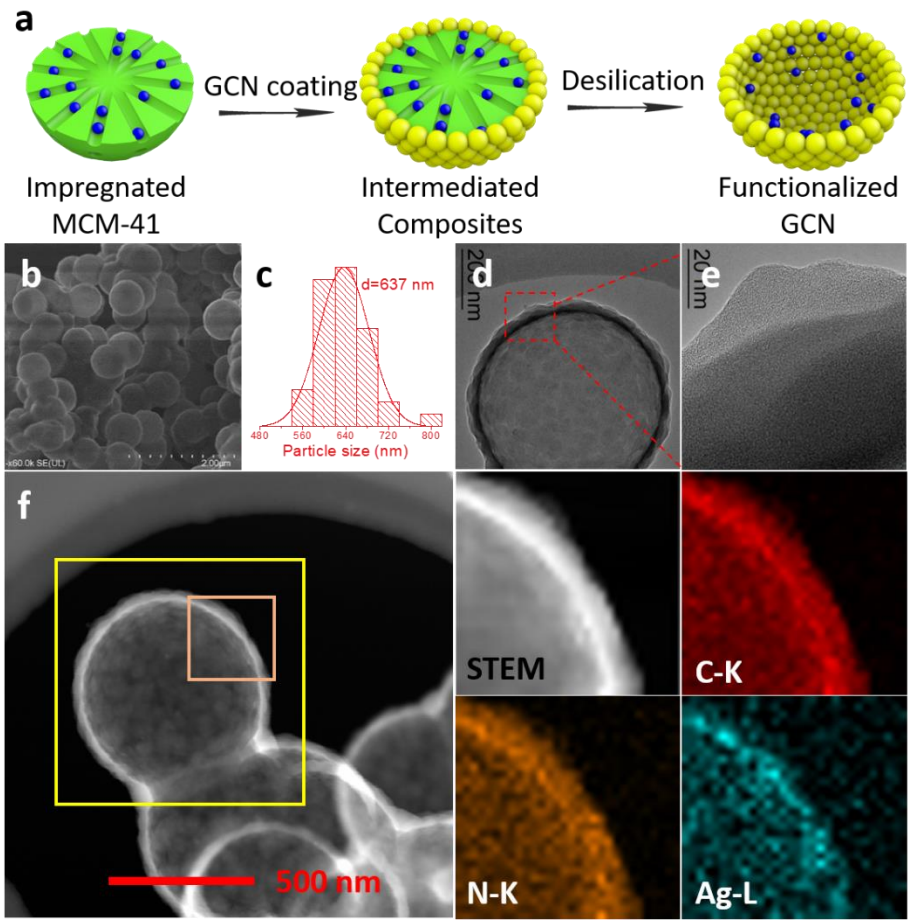

Figure 4. (a) Schematic illustration of the encapsulation for secondary component inside SSCN. (b) SEM, (c) particle size distribution, (d, e) TEM and (f) TEM-mapping images of Ag@SSCN

368 capsules.

369

370 The silver encapsulated g-C_3N_4 vesicle composites (coded as Ag@SSCN) are prepared through
371 the shape-selective templating method. Figure S12b-c shows the SEM image and the corresponding
372 particle size distribution of Ag@SSCN. As can be seen, Ag@SSCN exhibits the uniform 637 nm
373 spherical structure without bulk morphology, which further confirms that the solvent-free strategy is
374 universal for facile morphology controlling. The vesicle structure was characterized through TEM
375 (Figure S12d-e) and TEM-mapping (Figure S12f). As shown in Figure S12d-e, a similar vesicle
376 structure to SSCN was exhibited and no obvious silver nanoparticles were observed, indicating its
377 high dispersion. Furthermore, TEM-mapping images confirm the existence of carbon, nitride and
378 silver. Carbon and nitrogen are more evenly dispersed on the wall, while silver is more likely to be
379 dispersed inside the wall.

380

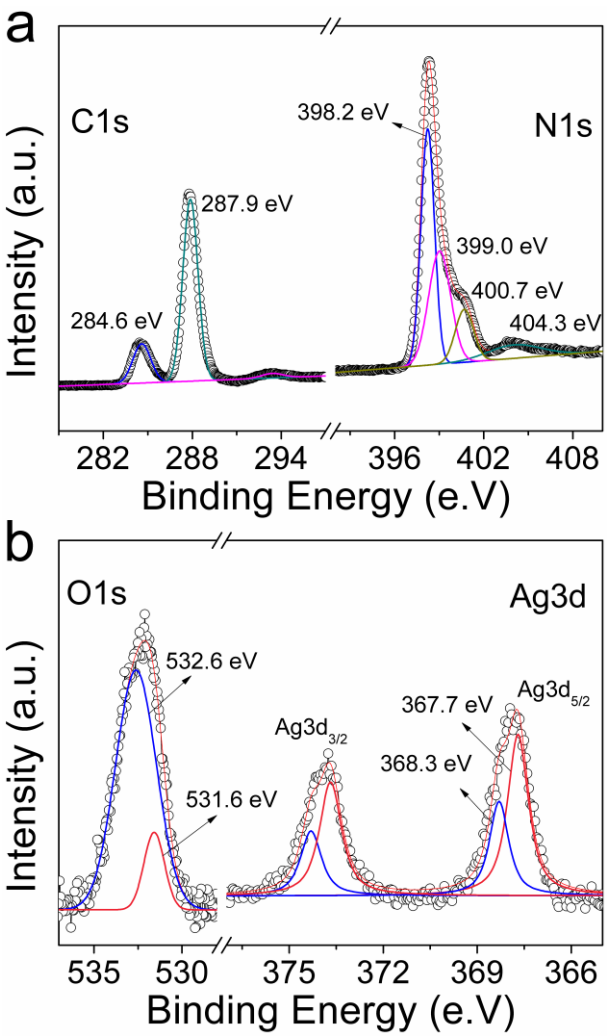

Figure S12. XPS spectra of Ag@SSCN: (a) C1s and N1s, (b) O1s and Ag3d.

Figure S12 presents the XPS spectra of Ag@SSCN. It can be seen from Figure S12a that the C1s and N1s XPS spectrum is corresponding with g-C_3N_4 as analyzed preciously. O1s peak (Figure S12b) can be divided into two peaks at 532.6 and 531.6 eV, which belong to lattice oxygen and adsorbed oxygen species, respectively. The $Ag3d_{5/2}$ XPS spectra can be divided into two peaks at 368.3 and 367.7 eV, which assigned to Ag^0 and Ag^+, respectively. The fitting results showed that the contents of Ag^0 and Ag^+ were 59.2% and 40.8%, respectively. The results show that the structure of Ag@SSCN retains the classical structure of g-C_3N_4 and the encapsulation of Ag is realized successfully.

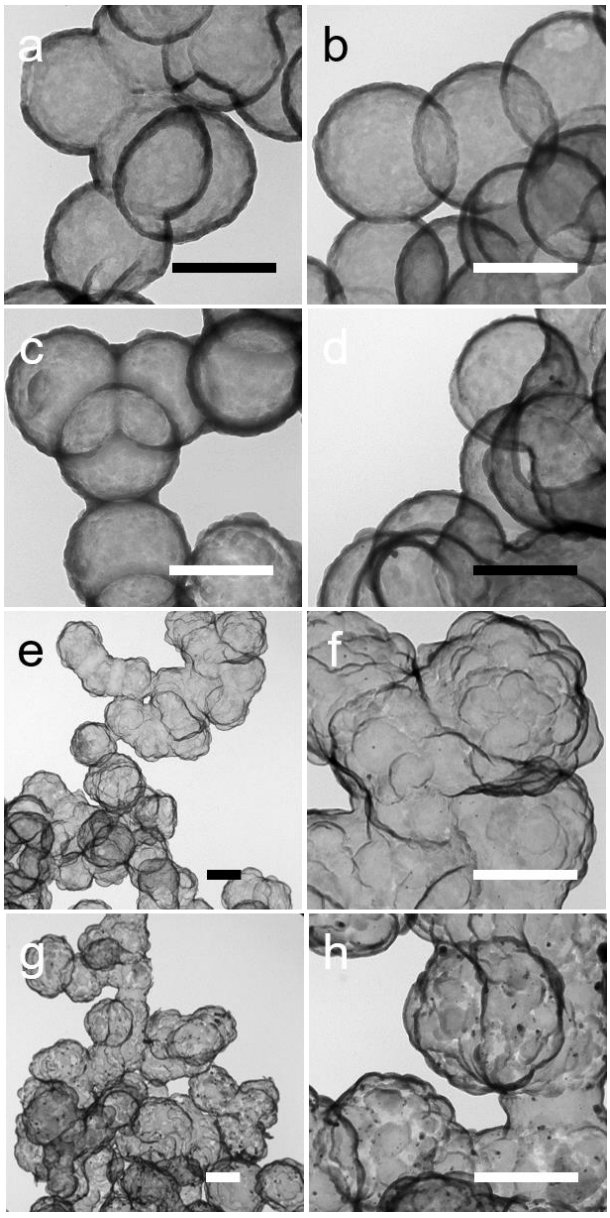

Figure S13. TEM images of (a) 0.3Ag@SSCN, (b) 1Ag@SSCN, (c) 3Ag@SSCN, (d) 6Ag@SSCN, (e, f) 10Ag@SSCN, (g, h) 15Ag@SSCN. The scale bar is 500 nm. The number in the sample code represents the mass ratio of silver in the template.

The content of the second metal component in the encapsulation of vesicles can be controlled through changing the impregnation amount of silver in the template. Figure S13 shows the TEM images of the encapsulated vesicles with different amounts of silver. It can be seen that when the content of silver in the template is lower than 6 wt%, the morphology of Ag@SSCN does not

change obviously, and it is still a thin single-shelled vesicle structure. At the same time, the presence of silver nanoparticles was not observed in TEM, indicating that silver is highly dispersed. When the content of silver in the template was higher than 10 wt%, the morphology of Ag@SSCN changed significantly, from regular vesicle structure to wrinkled vesicle structure. The wrinkled vesicle structure may provide more active sites for the reaction.

In addition to encapsulating noble metals, transition metal oxides can also be encapsulated through the identical strategy. The XPS spectra (Figure S14) of g-C_3N_4 vesicles encapsulated with transition metal oxides (Fe_2O_3, Co_2O_3, NiO and CuO) confirmed the existence of the corresponding metal oxides. From Figure S15, the encapsulated samples retain the intact nanocapsule structure of thin single-shell g-C_3N_4, which indicates that the introduction of metal oxides does not obviously affect the melamine polymerization to form g-C_3N_4 vesicles. At the same time, no obvious metal oxides were observed, indicating that the polymerization of metal oxides encapsulated by g-C_3N_4 vesicles was highly dispersed.

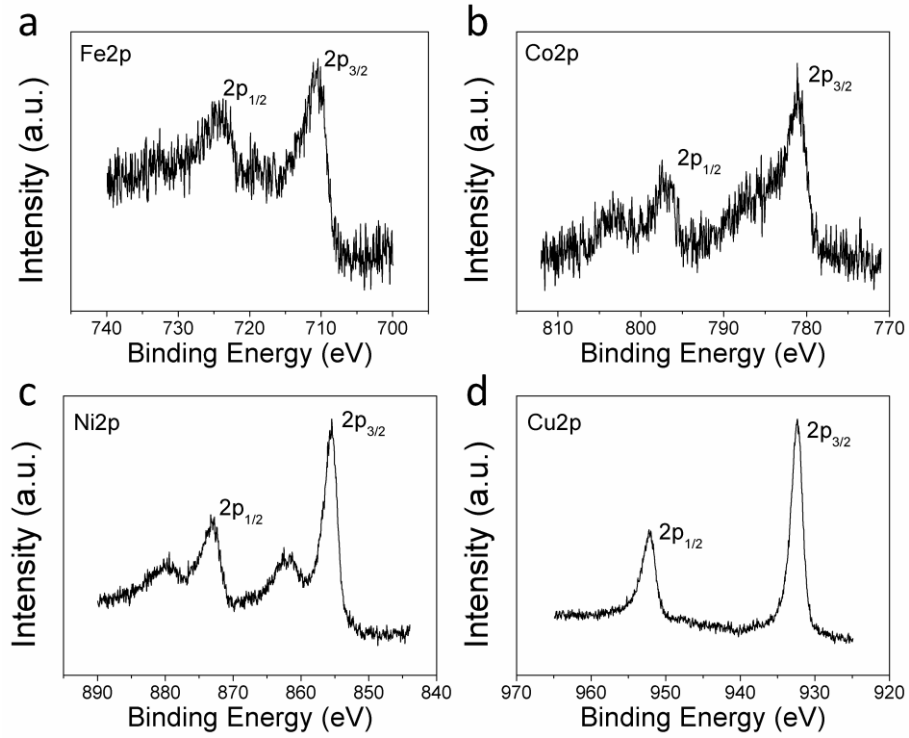

Figure S14. XPS spectra of (a) 3Fe@SSCN, (b) 3Co@SSCN, (c) 3Ni@SSCN and (d) 3Fe@SSCN.

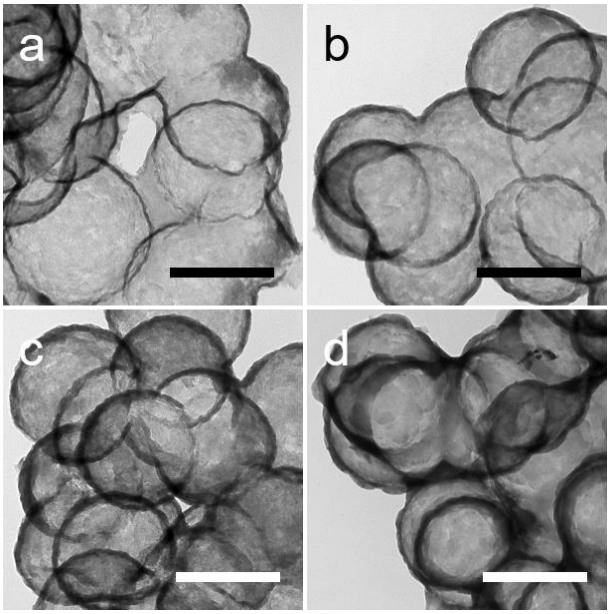

Figure S15. TEM images of (a) 3Fe@SSCN, (b) 3Co@SSCN, (c) 3Ni@SSCN and (d) 3Fe@SSCN. The scale bar is 500 nm.

Conclusions

In summary, we have developed a solvent-free shape-selective templating strategy to fabricate the pristine and functional g-C_3N_4 vesicles using melamine as precursor. The slightly larger channel (ca. 2.0 nm) than the dynamics diameter of melamine molecular (0.66 nm) allows its mass diffusion but prevents the polymerization inside the channel, and therefore enables the selective surface deposition and polymerization of melamine on the opened-up outer surface. The as-prepared single- and double-shelled g-C_3N_4 were composed of fragmental g-C_3N_4 nanosheets, which result in the enlarged surface area, shortened charge migration length and suppressed charge recombination efficiency. During the photocatalytic degradation of RhB and H_2 production reaction, double-shelled g-C_3N_4 exhibited almost 15.6 and 5.6 folds improvement when compared with the bulk one. The newly developed strategy provides a versatile and green method to solvent-free prepare various morphological and encapsulated g-C_3N_4 vesicles. Importantly, shape-selective preparation was applied in morphological evolution of g-C_3N_4 for the first time.

Methods

Reagents.

Melamine, Cetyltrimethyl ammonium bromide (CTAB), tetraethyl orthosilicate (TEOS) and $NH_3 \cdot H_2O$ (27 wt.%) were analysis grade and were used as obtained. Distilled water was used all the time.

Preparation of the MCM-41 and hollow MCM-41 nanoparticles.

The preparation of the spherical and hollow MCM-41 were followed according to the literature[38]. The stöber method was used to prepare the spherical MCM-41. The surface-protected etching method was used to prepare the hollow MCM-41. In a typical experiment, 1.0 g spherical

MCM-41 without calcination was suspended in 160 mL distilled water at 70 ºC. The suspension was stirred gently for 12 h to generate the hollow structure. The mechanism of the surface-protected etching method can be found in the literature[38]. Spherical and hollow MCM-41 were calcinated at 550 ºC for 6 h to eliminate CTAB for the latter preparation of morphological g-C_3N_4.

Preparation of single and double-shelled g-C_3N_4.

The shape-selective templating strategy was applied to fabricate the single- and double-shelled g-C_3N_4 vesicles based on the shape selectivity of the MCM-41 templates for melamine precursor. Though direct calcination the manually grinded mixtures of melamine and the silica templates, the morphological g-C_3N_4 were prepared. In a typical experiment for the preparation of the single-shelled g-C_3N_4, 1.0 g melamine and a certain amount of the spherical MCM-41 nanoparticles were grinded to uniform, followed by thermal polymerization at 550 ºC for 3 h at a heating rate of 10 ºC/min. After cooling down, the as-obtained yellow composites were treated with 4 M NH_4HF_2 aqueous solution to eliminate the silica templates. The solid was washed with water several times and dried in 100 ºC overnight. In the case of the double-shelled g-C_3N_4 preparation, identical process was conducted but with the hollow MCM-41 as the sacrificial templates. The as-obtained single- and double-shelled g-C_3N_4 were labelled with SSCN and DSCN.

Photocatalytic evaluation.

The visible light photocatalytic activity of the as-prepared samples were evaluated with photodegradation of RhB. Visible light comes from a 500 W Xe lamp with an optical cut-off filter ($\lambda > 420$ nm). In a typical experiment, 50 mg of the g-C_3N_4 were mixed with 50 mL RhB solution (50 mg/L) and ultrasonicated for 60 s. Before visible light irradiation, the suspension was stirred at 35 ºC in dark for 30 min to reach the adsorption-desorption equilibrium. After turning on the visible light, the suspension was sampled with 5 min intervals and centrifuged to measure the concentration

of RhB with ultraviolet spectrophotometer.

Characterization.

TEM images were taken on a Tecnai G2 20 S-twin instrument (FEI Company). The nitrogen sorption isotherms were measured with a Quantachrome autosorb-iQ2 gas adsorption analyzer at 77 K. XRD patterns were recorded on a Smart Lab 9 X-ray diffractometer (Rigaku Corporation). FT-IR spectra were measured an EQUINOX55 FT-IR spectrometer. XPS spectra were recorded on a Thermo VG ESCALAB250 instrument. Steady-state PL spectra were acquired on a JASCO FP-6200 spectrofluorometer with the excitation wavelength at 310 nm.

Acknowledgements.

This work was supported by the State Key Program of National Natural Science Foundation of China (grant no. 21306018), the QianRen program, and the Fundamental Research Funds for the Central Universities (Grant No. DUT16LK12).

Associated contents.

Supporting information

Figure S1. (a) N_2 physical adsorption-desorption isotherms at 77 K and (b) the pore size distribution of MCM-41 calculated by BJH method.

Figure S2. The TEM images of the identical MCM-41@g-C_3N_4 nanoparticle at different electron beam radiation time. The radiation time is gradually extended from a to d. The scale bar is 200 nm.

Figure S3. Structure and phase identification of BCN and SSCN. (a) XRD patterns, (b) FT-IR spectra, (c) C1s and N1s high resolution XPS spectra, (d) N2 physical adsorption-desorption isotherms at 77K and the pore size distribution calculated by BJH method

Figure S4. XRD patterns of g-C3N4/MCM-41 composites prepared under different temperatures.

Figure S5. The schematic illustration of the migration and polymerization of the carbon and nitrogen species in the presence of MCM-41.

Figure S6. (a, c) Nitrogen physical adsorption-desorption isotherms and (b, d) the pore size distribution of the core/shell silica and series of MS-x silica. The pore size distribution is calculated by the BJH method.

Figure S7. TEM images of (a, c, e) MS-1, MS-2 and MS-3, and (b, d, f) the as-templated g-C3N4.

Figure S8. TEM images

Figure S9. Single-shelled g-C3N4 vesicles prepared with different mass ratio of melamine/MCM-41. The ratio is (a) 0.1, (d) 0.3, (e) 0.5, (g) 0.8.

Figure S10. (a) N_2 physical adsorption-desorption isotherms at 77 K and (b) the pore size distribution of hollow MCM-41 calculated by BJH method.

Figure S11. Steady-state photofluorescence spectra of BCN, SSCN and DSCN.

Figure S12. XPS spectra of Ag@SSCN: (a) C1s and N1s, (b) O1s and Ag3d.

Figure S13. TEM images of (a) 0.3Ag@SSCN, (b) 1Ag@SSCN, (c) 3Ag@SSCN, (d) 6Ag@SSCN, (e, f) 10Ag@SSCN, (g, h) 15Ag@SSCN. The scale bar is 500 nm.

Figure S14. XPS spectra of (a) 3Fe@SSCN, (b) 3Co@SSCN, (c) 3Ni@SSCN and (d) 3Fe@SSCN.

Figure S15. TEM images of (a) 3Fe@SSCN, (b) 3Co@SSCN, (c) 3Ni@SSCN and (d) 3Fe@SSCN. The scale bar is 500 nm.

Table S1. Textual properties and elemental composition of samples BCN, SSCN and DSCN.

Table S2. The phase of the products obtained from melamine polymerization with MCM-41 or without MCM-41 at different temperatures.

Table S3. Textural properties of the core/shell silica and series of MS-x silica.

Error! Reference source not found.

References.

[1] X. Wang, K. Maeda, A. Thomas, K. Takanabe, G. Xin, J.M. Carlsson, K. Domen, M. Antonietti, A metal-free polymeric photocatalyst for hydrogen production from water under visible light, Nat. Mater., 8 (2009) 76-80.

[2] Y. Zheng, L. Lin, B. Wang, X. Wang, Graphitic Carbon Nitride Polymers toward Sustainable Photoredox Catalysis, Angew. Chem. Int. Ed., 54 (2015) 12868-12884.

[3] W.J. Ong, L.-L. Tan, Y.H. Ng, S.-T. Yong, S.-P. Chai, Graphitic Carbon Nitride ($g\text{-}C_3N_4$)-Based Photocatalysts for Artificial Photosynthesis and Environmental Remediation: Are We a Step Closer To Achieving Sustainability?, Chem. Rev., 116 (2016) 7159-7329.

[4] Y. Zheng, Y. Jiao, M. Jaroniec, Y. Jin, S.Z. Qiao, Nanostructured metal-free electrochemical catalysts for highly efficient oxygen reduction, Small, 8 (2012) 3550-3566.

[5] D.T. Martin, K. Qiu, S.A. Shevlin, A.D. Handoko, X. Chen, Z. Guo, J. Tang, Highly Efficient Photocatalytic H_2 Evolution from Water Light and Structure Controlled Graphitic Carbon Nitride using Visible, Angew. Chem. Int. Ed., 126 (2014) 9394-9399.

[6] D.J. Martin, P.J. Reardon, S.J. Moniz, J. Tang, Visible light-driven pure water splitting by a nature-inspired organic semiconductor-based system, J. Am. Chem. Soc., 136 (2014) 12568-12571.

[7] G. Zhang, Z.A. Lan, X. Wang, Surface engineering of graphitic carbon nitride polymers with cocatalysts for photocatalytic overall water splitting, Chemical Science, 8 (2017) 5261-5274.

[8] G. Zhang, Z.-a. Lan, X. Wang, Conjugated Polymers:Catalysts for Photocatalytic Hydrogen Evolution, Angew. Chem. Int. Ed., 55 (2016) 15712.

[9] S.J.A. Moniz, S.A. Shevlin, D.J. Martin, Z.-X. Guo, J. Tang, Visible-light driven heterojunction photocatalysts for water splitting – a critical review, Energy Environ. Sci., 8 (2015) 731-759.

[10] K. Wang, Q. Li, B. Liu, B. Cheng, W. Ho, J. Yu, Sulfur-doped $g\text{-}C_3N_4$ with enhanced photocatalytic CO_2-reduction performance, Appl. Catal. B-Environ, 176-177 (2015) 44-52.

[11] P. Niu, Y. Yang, J.C. Yu, G. Liu, H.M. Cheng, Switching the selectivity of the photoreduction reaction of carbon dioxide by controlling the band structure of a g-C3N4 photocatalyst, Chem. Commun., 50 (2014) 10837-10840.

[12] W. Yu, D. Xu, T. Peng, Enhanced photocatalytic activity of g-C3N4 for selective CO2 reduction to CH3OH via facile coupling of ZnO: a direct Z-scheme mechanism, J. Mater. Chem. A, 3 (2015) 19936-19947.

[13] Y. Zhang, Z. Zhou, Y. Shen, Q. Zhou, J. Wang, A. Liu, S. Liu, Y. Zhang, Reversible Assembly of Graphitic Carbon Nitride 3D Network for Highly Selective Dyes Absorption and Regeneration, ACS Nano, 10 (2016) 9036-9043.

[14] X. Wang, X. Chen, A. Thomas, X. Fu, M. Antonietti, Metal-Containing Carbon Nitride Compounds: A New Functional Organic-Metal Hybrid Material, Adv. Mater., 21 (2009) 1609-1612.

[15] Z. Tong, D. Yang, Z. Li, Y. Nan, F. Ding, Y. Shen, Z. Jiang, Thylakoid-Inspired Multishell $g\text{-}C_3N_4$ Nanocapsules with Enhanced Visible-Light Harvesting and Electron Transfer Properties for High-Efficiency Photocatalysis, ACS Nano, 11 (2017) 1103-1112.

[16] Q. Han, B. Wang, J. Gao, Z. Cheng, Y. Zhao, Z. Zhang, L. Qu, Atomically Thin Mesoporous Nanomesh of Graphitic-C_3N_4 for High-efficiency Photocatalytic Hydrogen Evolution, ACS Nano, 10 (2016) 2745.

[17] Z. Zhou, Y. Shen, Y. Li, A. Liu, S. Liu, Y. Zhang, Chemical cleavage of layered carbon nitride with enhanced photoluminescent performances and photoconduction, ACS Nano, 9 (2015) 12480-12487.

[18] B.V. Lotsch, W. Schnick, New light on an old story: formation of melam during thermal condensation of melamine, Chemistry, 13 (2007) 4956-4968.

[19] M.B. Ansari, B.-H. Min, Y.-H. Mo, S.-E. Park, CO_2 activation and promotional effect in the oxidation of cyclic olefins over mesoporous carbon nitrides, Green Chem., 13 (2011) 1416-1421.

[20] J. Chen, Z. Mao, L. Zhang, D. Wang, R. Xu, L. Bie, B.D. Fahlman, Nitrogen-Deficient Graphitic Carbon Nitride with Enhanced Performance for Lithium Ion Battery Anodes, ACS Nano, 11 (2017) 12650-12657.
[21] L. Shi, L. Liang, F. Wang, M. Liu, K. Chen, K. Sun, N. Zhang, J. Sun, Higher Yield Urea-Derived Polymeric Graphitic Carbon Nitride with Mesoporous Structure and Superior Visible-Light-Responsive Activity, ACS Sustain. Chem. Eng., 3 (2015) 3412-3419.
[22] J. Xu, Y. Wang, Y. Zhu, Nanoporous graphitic carbon nitride with enhanced photocatalytic performance, Langmuir, 29 (2013) 10566-10572.
[23] D.J. Martin, K. Qiu, S.A. Shevlin, A.D. Handoko, X. Chen, Z. Guo, J. Tang, Highly Efficient Photocatalytic H_2 Evolution from Water using Visible Light and Structure-Controlled Graphitic Carbon Nitride, Angew. Chem. Int. Ed., 53 (2014) 9240-9245.
[24] C. Dai, A. Zhang, M. Liu, L. Gu, X. Guo, C. Song, Hollow Alveolus-Like Nanovesicle Assembly with Metal-Encapsulated Hollow Zeolite Nanocrystals, ACS Nano, 10 (2016) 7401-7408.
[25] C. Dai, A. Zhang, M. Liu, X. Guo, C. Song, Hollow ZSM-5 with Silicon-Rich Surface, Double Shells, and Functionalized Interior with Metallic Nanoparticles and Carbon Nanotubes, Adv. Funct. Mater., 25 (2015) 7479-7487.
[26] D. Zheng, G. zhang, X. Wang, Integrating CdS quantum dots on hollow graphitic carbon nitride nanospheres for hydrogen evolution photocatalysis, Appl. Catal. B-Environ, 179 (2015) 479-488.
[27] J. Sun, J. Zhang, M. Zhang, M. Antonietti, X. Fu, X. Wang, Bioinspired hollow semiconductor nanospheres as photosynthetic nanoparticles, Nat. Commun., 3 (2012) 1139-1145.
[28] L. Zhou, Z. Zhuang, H. Zhao, M. Lin, D. Zhao, L. Mai, Intricate Hollow Structures: Controlled Synthesis and Applications in Energy Storage and Conversion, Adv. Mater., 29 (2017) 1602914.
[29] B. Qiu, Q. Zhu, M. Du, L. Fan, M. Xing, J. Zhang, Efficient Solar Light Harvesting CdS/Co_9S_8 Hollow Cubes for Z-scheme photocatalytic water splitting, Angew. Chem. Int. Ed., 56 (2017) 2684-2688.
[30] Y. Zhao, L. Jiang, Hollow Micro/Nanomaterials with Multilevel Interior Structures, Adv. Mater., 21 (2009) 3621-3638.
[31] X. Wang, Y. Zhang, W. Luo, A.A. Elzatahry, X. Cheng, A. Alghamdi, A.M. Abdullah, Y. Deng, D. Zhao, Synthesis of Ordered Mesoporous Silica with Tunable Morphologies and Pore Sizes via a Nonpolar Solvent-Assisted Stöber Method, Chem. Mater., 28 (2016) 2356-2362.
[32] X. Du, S.Z. Qiao, Dendritic Silica Particles with Center-Radial Pore Channels: Promising Platforms for Catalysis and Biomedical Applications, Small, 11 (2015) 392-413.
[33] J. Zhang, M. Zhang, C. Yang, X. Wang, Nanospherical carbon nitride frameworks with sharp edges accelerating charge collection and separation at a soft photocatalytic interface, Adv. Mater., 26 (2014) 4121-4126.
[34] Y. Yang, X. Liu, X. Li, J. Zhao, S. Bai, J. Liu, Q. Yang, A yolk-shell nanoreactor with a basic core and an acidic shell for cascade reactions, Angewandte Chemie, 51 (2012) 9164-9168.
[35] D. Zheng, X.N. Cao, X. Wang, Precise Formation of a Hollow Carbon Nitride Structure with a Janus Surface to Promote Water Splitting by Photoredox Catalysis, Angewandte Chemie, (2016).
[36] Q. Zhang, D.Q. Lima, I. Lee, F. Zaera, M. Chi, Y. Yin, A highly active titanium dioxide based visible-light photocatalyst with nonmetal doping and plasmonic metal decoration, Angewandte Chemie, 50 (2011) 7088-7092.
[37] D. Wang, T. Hisatomi, T. Takata, C. Pan, M. Katayama, J. Kubota, K. Domen, Core/Shell photocatalyst with spatially separated co-catalysts for efficient reduction and oxidation of water, Angewandte Chemie, 52 (2013) 11252-11256.
[38] Z. Teng, X. Su, Y. Zheng, J. Sun, G. Chen, C. Tian, J. Wang, H. Li, Y. Zhao, G. Lu, Mesoporous Silica Hollow Spheres with Ordered Radial Mesochannels by a Spontaneous Self-Transformation Approach, Chem. Mater., 25 (2013) 98-105.
[39] B. Smit, Molecular Simulations of Zeolites : Adsorption, Diffusion and Shape Selectivity, Chem. Rev., 108 (2008) 4125.
[40] J. Qin, S. Wang, H. Ren, Y. Hou, X. Wang, Photocatalytic reduction of CO_2 by graphitic carbon nitride polymers derived from urea and barbituric acid, Appl. Catal. B-Environ, 179 (2015) 1-8.

603 [41] S. Cao, J. Low, J. Yu, M. Jaroniec, Polymeric photocatalysts based on graphitic carbon nitride, Adv. Mater., 27 (2015)
604 2150-2176.
605 [42] S.C. Yan, Z.S. Li, Z.G. Zou, Photodegradation performance of g-C_3N_4 fabricated by directly heating melamine,
606 Langmuir, 25 (2009) 10397-10401.
607 [43] H. Li, Z. Bian, J. Zhu, D. Zhang, G. Li, Y. Huo, H. Li, Y. Lu, Mesoporous Titanic Spheres with Tunable Chamber
608 Stucture and Enhanced Photocatalytic Activity, J. Am. Chem. Soc., 129 (2007) 8406.

609